Comput. Mech. (2007) 39: 381–399
DOI 10.1007/s00466-006-0035-z

ORIGINAL ARTICLE

**Rodrigo Rossi · Marcelo Krajnc Alves**

# On the analysis of an EFG method under large deformations and volumetric locking

Received: 2 May 2005 / Accepted: 11 January 2006 / Published online: 23 February 2006
© Springer-Verlag 2006

**Abstract** This work investigates a modified element-free Galerkin (MEFG) method when applied to large deformation processes. The proposed EFG method enables the direct imposition of the essential boundary conditions, as a result of the kronecker delta property of the special shape functions, constructed in the neighborhood of the essential boundary. The plasticity model assumes a multiplicative decomposition of the deformation gradient into an elastic and a plastic part and considers a $J_2$ elasto-plastic constitutive relation that accounts for a nonlinear isotropic hardening. The constitutive model is written in terms of the rotated *Kirchhoff* stress and of the conjugate logarithmic strain measure. A total Lagrangian formulation is considered in order to improve the computational performance of the proposed algorithm. Here, aspects related to the volumetric locking are numerically investigated and an *F-bar* approach is considered. Some numerical results are presented, under axisymmetric and plane strain assumption, in order to attest the performance of the proposed method.

**Keywords** Finite strains · Mesh-free · EFG · Volumetric locking

Rodrigo Rossi (✉)
Departamento de Engenharia Mecânica,
Universidade de Caxias do Sul
Cidade Universitária,
Caxias do Sul,
RS 95070-560, Brazil
E-mail: rrossi@ucs.br
Tel.: +55-54-2181133
Fax: +55-54-2182168

Marcelo Krajnc Alves
Departamento de Engenharia Mecânica,
Universidade Federal de Santa Catarina,
Campus Trindade,
Florianópolis,
SC 88010-970 Brazil
E-mail: krajnc@emc.ufsc.br
Tel.: +55-48-3319264
Fax: +55-48-2343131

## 1 Introduction

Large deformation analysis has an important role and a key place in solid mechanics science. Many physical phenomena that occur in industrial processes, as for instance in metal forming, require its usage and, in general, a large amount of plastic deformation. Despite the small deformation analysis, where the deformation measure is universal, given by $\boldsymbol{\varepsilon}(\boldsymbol{u}) = \nabla_S \boldsymbol{u}$, the formulation in finite strains offers a wide variety of possibilities. Different deformation measures such as the *Lagrangian* measures; based on the right *Cauchy–Green* tensor $\mathbf{U}$, and the *Eulerian* measures, based on the left *Cauchy–Green* tensor $\mathbf{V}$, together with their conjugate stresses, may be employed in the finite deformation framework.

In this work, the (MEFG) modified element free Galerkin method, which combines the Element EFG with an extended Partition of unity finite element method (PUFEM), allowing the enforcement, in some limiting sense, of the essential boundary conditions as done in the finite element method (FEM), will be numerically investigated when applied to large deformation problems. (see Alves and Rossi [2]).

The proposed extended PUFEM is based in the moving least square approximation (MLSA) and overcomes singularity problems, in the global shape functions, resulting from the usage of a conventional PUFEM together with linear and higher order base functions. In order to avoid the presence of singular points, the extended PUFEM considers an extension of the support of the classical PUFE weight function. Moreover, since the extended PUFEM is closely related to the EFG method, no need of special approximation functions with complex implementation procedures is necessary and no use of the penalty and/or multiplier method is required in order to approximately impose the essential boundary condition. Thus, a relatively simple procedure is necessary in order to combine both methods.

The extension of the modified EFG to finite deformation considers:

- A *Total Lagrangian* description;

- A multiplicative decomposition of the deformation gradient, into a plastic and an elastic part;
- A constitutive relation, given in terms of the logarithmic deformation measure, ln($\mathbf{U}$), and the conjugate rotated *Kirchhoff* stress measure. In this model the elastic response is assumed to be hyperelastic, according to the Hencky model, and the plastic flow is described by a $J_2$ plasticity model.

The use of the rotated *Kirchhoff* stress together with the logarithmic deformation measure was initially described in Eterovic and Bathe [10] and Weber and Anand [32], and also employed by Akkaram and Zabaras [1] among others. Similar investigations, employing however an Eulerian description using the *Kirchhoff* stress and the logarithmic deformation measure, ln($\mathbf{V}$), were also presented in Souza Neto et al. [28, 29].

The choice of these above conjugate stress-strain pairs in the formulation of the constitutive equation leads to a return mapping that is described in the same form as the one found in the small deformation plasticity schemes. This allows the incorporation of elastoplastic material models, derived in the small deformation scope, into large deformation algorithms in a simple and direct way.

The $J_2$ plasticity model considered in the work assumes that the plastic deformation process is incompressible. This incompressibility hypothesis leads to the so called volumetric locking phenomenon, which occurs for instance, whenever a low order finite element interpolation is used, when solving plane strains and axisymmetric problems. Such phenomenon is also verified in mesh-free methods as mention in Askes et al. [4], Dolbow and Belytschko [8], and Huerta and Méndez [16].

The *B-bar* method $\left(\bar{B}\right)$ proposed by Hughes [17], the enhanced assumed strain (EAS) method proposed by Simo and Rifai [27] and the *F-bar* method $\left(\bar{\mathbf{F}}\right)$ proposed by Souza Neto et al. [28] are examples of methodologies largely used in the literature in order to circumvent the volumetric locking phenomenon, when using low order finite elements. These methodologies are formulated in a general frame work and may be applied, without significant changes, to the MEFG method.

More specifically, on the volumetric locking phenomenon in EFG methods, some procedures were proposed in order to cope with the problem. Wells et al. [29] propose that a local extrinsic enrichment be accomplished just where the plastic flow takes place. Vidal et al. [31] proposes a pseudo-divergence-free approach, which consists in using shape functions that verify approximately the divergence-free constraint. In Askes et al. [4], it is numerically shown, for near incompressible solids, that the volumetric locking problem is not evidenced if a sufficiently large support of the global shape function is used. However, Huerta and Méndez [15], show that the volumetric locking problem is just attenuated, but not suppressed from the analysis. Mixed formulations, where the displacements and pressure fields are approximated separately, are also proposed in the literature in the context of mesh-free methods, together with strategies of selective integration. In this case the *inf–sup* condition of *Ladyzhenskaya–Brezi–Babuska* (LBB) must be satisfied. See Dolbow and Belytschko [8].

This work presents a variation of the *F-bar* method $\left(\bar{\mathbf{F}}\right)$, which is implemented in the context of the modified EFG method and investigated under axisymmetric and plane strain conditions. The choice of selecting an *F-bar* approach is due to the simplicity of its implementation, when compared to the other proposed strategies, and the good results obtained by Souza Neto et al. [28, 29] and Akkaram and Zabaras [1].

## 2 A brief description of the modified element-free Galerkin method

### 2.1 Introduction

In the last 10 years a considerable attention has been given to the so-called "meshless or mesh-free methods". This new class of numerical methods is being applied to solve engineering problems, where the traditional numerical methods face difficulties, such as in large deformation problems.

Naturally, together with these new methods new problems have originated, such as the need to: implement appropriate numerical integration schemes; enforce essential boundary conditions; and reduce the computational cost, when compared with the traditional finite element method, among others.

Here, the focus is on the extension of the MEFG method, which proposes a novel method to impose the essential boundary conditions, to large deformation problems and the reduction of the computational cost of the method. The computational cost may be considerably reduced if one considers:

- the formulation of the problem in the *Total Lagrangian* framework, which allows the implementation of simple procedures, such as computing only once and storing in memory the matrices containing the global interpolation functions and their derivatives at each integration points;
- the investigation of effective and low computational cost methods for coping with the existing volumetric locking problems.

The need of special procedures for the imposition of the essential boundary conditions, in the scope of the EFG method, arises from the fact that the resulting shape functions do not satisfy the kronecker delta property. Several distinct approaches have been proposed in the literature to overcome this problem. Among them are: the usage of collocation methods Belytschko and Tabbara [5], and Zhu and Atluri [35], the usage of Lagrange multiplier methods Belytschko et al. [6], the combination of EFG with the FEM Belytschko et al. [7], Krongauz and Belytschko [19], Hegen [13] and Huerta and Méndez [15], the usage of singular weight functions Duarte and Oden [9] and Kaljević and Saigal [17], and the application of penalty methods Zhu and Atluri [35]. Some other approaches and variations can also be found in Günther and Liu [12], Pannachet and Askes [23], Gavete et al. [11], Zhang et al. [34] and Ventura [30].

Each of these methods presents some advantages and drawbacks. Lagrange multiplier methods are commonly used and are effective to impose constraints on optimization problems. Nevertheless, their use present some disadvantages such as: the ill conditioning of the resulting algebraic system of equations, the increase in the problem size, and the inability to impose the essential boundary conditions with a high degree of accuracy as mentioned in Belytschko et al. [6].

Methods that combine EFG with FEM, such as Belytschko et al. [7], Krongauz and Belytschko [19], Hegen [13] and Huerta and Méndez [15], make use of a mixed interpolation approach requiring both finite elements and EFG base functions. Thus the domain must be decomposed in two sub domains, one defined by a set of nodes with their associate FE shape functions and the other defined by a set of particles with their associated EFG shape functions. Moreover, in the transition domain, where the support of both EFG and FE base functions overlap, the global approximation is decomposed as a sum of a FE and EFG global shape functions what requires, in order for satisfying the consistency conditions, some special procedures, making it difficult to be implemented and generalized.

The use of singular weight functions has the drawback of been highly non-polynomial, as shown in Hegen [13], and are responsible for a loss in accuracy, if an inadequate integration scheme is employed. Also, the enforcement of the essential boundary conditions are only achieved at the center of the singular weight functions. In addition, results obtained from penalty methods are parameter dependent and Collocation methods are in general inappropriate, see Zhu and Atluri [35].

Here, the imposition of the essential boundary conditions is performed by the introduction of a weight function derived from, an extended PUFEM (EPUFEM). This EPUFEM will act only at the neighborhood of the essential boundary. Thus, the remaining domain is covered by traditional EFG weight functions. Also, since both EFG shape functions and EPUFE shape functions are derived from the MLSA approach using the same intrinsic base, the consistency condition is naturally satisfied in the transition domain. Thus, the MEFG method can be seen as a conventional EFG method, containing a set of different weight functions, with the ability to identify at each particle the proper type of weight function and to determine the adequate size of its support.

## 2.2 Moving least square approximation

With the usage of the *Moving Least Square Approximation*, presented by Lancaster and Salkuskas [20], it is possible to construct an approximation function $u^h(\boldsymbol{X})$ that fits a discrete set of data $\{u_I,\ I = 1, \ldots, n\}$ so that:

$$u^h(X) = \sum\nolimits_{I=1}^{n} \Phi_I(\boldsymbol{X}) u_I, \tag{1}$$

$$\Phi_I(\boldsymbol{X}) = \boldsymbol{p}(\boldsymbol{X}) \cdot \mathbf{A}(\boldsymbol{X})^{-1} \boldsymbol{b}_I(\boldsymbol{X}), \tag{2}$$

$$\mathbf{A}(\boldsymbol{X}) = \sum_{I=1}^{n} w(\boldsymbol{X} - \boldsymbol{X}_I)[\boldsymbol{p}(\boldsymbol{X}_I) \otimes \boldsymbol{p}(\boldsymbol{X}_I)] \tag{3}$$

and

$$\boldsymbol{b}_I(\boldsymbol{X}) = w(\boldsymbol{X} - \boldsymbol{X}_I)\boldsymbol{p}(\boldsymbol{X}_I), \tag{4}$$

where $\left\{p_j(\boldsymbol{X}),\ j = 1, \ldots, m\right\}$ represents the set of intrinsic base functions and $w(\boldsymbol{X} - \boldsymbol{X}_I)$ represents a weight function centered at $\boldsymbol{X}_I$. Here, $\Phi_I(\boldsymbol{X})$ is the global shape function, defined at particle $\boldsymbol{X}_I$, and $\mathbf{A}(\boldsymbol{X})$ is the moment matrix.

## 2.3 Element-free Galerkin

The conventional EFG method, see Belytschko et al. [6], is described by the procedure that constructs the set of global shape functions, $\Phi_I(\boldsymbol{X})$, defined at each particle $\boldsymbol{X}_I$, which defines the approximation space. These global shape functions are then used together with the *Galerkin* method to solve the boundary value problem. The particles distribution, which defines how the covering of the domain is done by the global shape functions $\Phi_I(\boldsymbol{X})$, is not arbitrary since it must satisfy the following stability condition:

$$\text{card}\{\boldsymbol{X}_J\,|\Phi_J(\boldsymbol{X}) \neq 0\} \geq \dim\,[\mathbf{A}(\boldsymbol{X})]. \tag{5}$$

Thus, the number of particles $\boldsymbol{X}_J$ who's associated shape function $\Phi_J(\boldsymbol{X})$ have a nonzero value at $\boldsymbol{X}$, must be larger than the size of $\mathbf{A}(\boldsymbol{X})$, which is given by the number of intrinsic base functions in $\boldsymbol{p}(\boldsymbol{X})$. Moreover, for each $\boldsymbol{X} \in R^n$, there must be $n + 1$ particles, whose position vectors form a non-zero *nth* rank simplex element, Liu et al. [21]. Here, since $\boldsymbol{X} \in R^2$, with $\boldsymbol{X} = (X, Y)$, and the intrinsic base functions is $\boldsymbol{p}^{\mathrm{T}}(\boldsymbol{X}) = [1, X, Y]$ then, from (5), for all $\boldsymbol{X} \in \bar{\Omega}$, there must be at least three particles whose weight functions have a nonzero value at $\boldsymbol{X}$ and whose position vector forms a triangle with a non-zero area. Notice that, since the MLSA reproduces exactly the intrinsic base functions in $\boldsymbol{p}(\boldsymbol{X})$, the consideration of a linear intrinsic base ensures the satisfaction of the classical patch test.

In order to obtain a particle distribution that comply with (5), one performs a partition of the domain, $\Omega_o$, into a triangular integration mesh, where one considers each triangular partition/element to be an integration cell and each vertex node to be the position of a particle.

### *2.3.1 Element-free Galerkin weight functions*

One of the most common weight functions, used in the conventional EFG method, is the quartic-spline function, denoted here by $w^{\mathrm{EFG}}$ and given as:

$$w^{\mathrm{EFG}}(r) = \begin{cases} 1 - 6r^2 + 8r^3 - 3r^4, & \text{for}\, r \leq 1.0 \\ 0, & \text{for}\, r > 1.0. \end{cases} \tag{6}$$

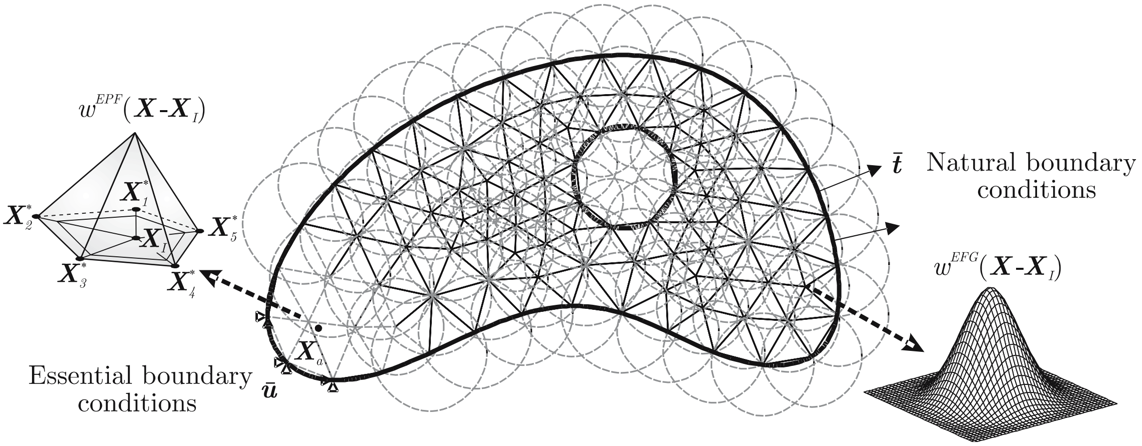

**Fig. 1** An example of body coverage by the MEFG

Here, $r = r_I/\bar{r}_I$ with $r_I = \|\boldsymbol{X} - \boldsymbol{X}_I\|$. The radius $\bar{r}_I$, defining the support of $w^{\mathrm{EFG}}(\boldsymbol{X} - \boldsymbol{X}_I)$, is determined by

$$\bar{r}_I = s \cdot r_{I\,\max}, \quad s > 1 \; s \in R \tag{7}$$

and

$$r_{I\,\max} = \max_i \|\boldsymbol{X}_i - \boldsymbol{X}_I\|, \quad i \in J_I, \tag{8}$$

where $J_I$ represents the set of adjacent nodes associated with $\boldsymbol{X}_I$. Here, one considers $s$=1.5, what assures a covering of the entire domain. The selection of the proper parameter $s$, which characterizes the support size, was based on the results of a parametric analysis performed in Rossi and Alves [24, 25].

Now, since the global shape functions $\{\Phi_I(\boldsymbol{X}), I = 1, \ldots, n\}$ do not satisfy, in general, the kronecker delta property, $\Phi_I(\boldsymbol{X}_j) \neq \delta_{IJ}$, it is not possible to enforce the essential boundary conditions, by directly prescribing nodal values, as done in the FEM. However, special weight functions may be constructed in order to satisfy the kronecker delta property. Among the possible weight functions is the extended partition of unity finite element (EPuFe) weight function.

### 2.4 Extended partition of unity finite element weight functions

The global shape functions $\{\Phi_I(\boldsymbol{X}), I = 1, \ldots, n\}$, employed in EPuFe, are also obtained by the use of the MLSA. A typical support of an EPuFe global shape function is illustrated in Fig. 1, where one can identify the adjacent extended node list of $\boldsymbol{X}_I$ given by the set $\boldsymbol{X}_1^*$, $\boldsymbol{X}_2^*$, $\boldsymbol{X}_3^*$, $\boldsymbol{X}_4^*$, $\boldsymbol{X}_5^*$. Now, at particles where a linear triangular finite element type of function is used as a weight function in the MLSA, it is possible derive:

$$w^{\mathrm{EPF}}(\boldsymbol{X}-\boldsymbol{X}_I)=\begin{cases}\frac{1}{2A}\left[\left(X_i^* Y_{i+1}^* - X_{i+1}^* Y_i^*\right)\right.\\ \left.+\left(Y_i^* - Y_{i+1}^*\right)X + \left(X_{i+1}^* - X_i^*\right)Y\right], \\ \qquad \boldsymbol{X} \in \operatorname{supp}\left[\Phi_I(\boldsymbol{X})\right] \\ 0, \quad \text{otherwise}\end{cases} \tag{9}$$

Here, $\boldsymbol{X}_i^*$ and $\boldsymbol{X}_{i+1}^*$ are the elements of the adjacent extended node list set of $\boldsymbol{X}_I$, obtained in a counter clockwise sense of the triangular integration cell whose area is $A$. The usage of an intrinsic base $\boldsymbol{p}^{\mathrm{T}}(\boldsymbol{X}) = [1, X, Y]$ together with a EPuFe weight function satisfy the requirement in (5) and, therefore, ensures the regularity of the moment matrix $\mathbf{A}(\boldsymbol{X})$. The extended points are determined as:

$$\boldsymbol{X}_i^* = \boldsymbol{X}_i + \varepsilon(\boldsymbol{X}_i - \boldsymbol{X}_I). \tag{10}$$

Notice that, letting $\varepsilon \to 0$, one derives a global shape function that satisfy, in a limiting sense, at a given particle $\boldsymbol{X}_J$, the kronecker delta property, i.e.

$$\lim_{\varepsilon \to 0} \Phi_I(\boldsymbol{X}_J) = \delta_{IJ}. \tag{11}$$

As a consequence, one may imposes the essential boundary conditions in the same way as done in the traditional FEM. Moreover, the error in the imposition of the essential boundary condition can be made as small as required, provided one uses a sufficiently small extension parameter$\epsilon$. Here, it's important to notice that, for a finite$\varepsilon$, a small violation of the kronecker delta condition occurs, i.e., there is a small violation of the prescribed essential boundary condition.

### 2.5 Modified element-free Galerkin method

The objective of the MEFG method is to combine, in a suitable way, both weight functions, in order to explore the smoothness of $w^{\mathrm{EFG}}$ and the kronecker delta property of $w^{\mathrm{EPF}}$. The strategy is shown by considering a body with domain $\Omega_o$ and boundary $\partial\Omega_o$, where $\partial\Omega_o = \Gamma_u \cup \Gamma_t$ and $\Gamma_u \cap \Gamma_t = \emptyset$. Here, $\Gamma_u$ and $\Gamma_t$ are respectively the part of $\partial\Omega_o$ with prescribed essential and natural boundary conditions, as illustrated in Fig. 1. Notice that the EPuFe weight functions are specified at particles that belong to a neighborhood of $\Gamma_u$ and the EFG weight functions are specified at the remaining particles of the mesh. This procedure enables the determination of an approximate solution that satisfies accurately the essential boundary condition and is smooth in the entire domain, except for a neighborhood of $\Gamma_u$.

The advantage of using EFG weight functions relies in the fact that the derived global shape functions are weakly depended on the selected integration mesh, when compared with the traditional FEM. This characteristic allows mesh free methods to withstand very large deformations before any numerical ill-conditioning takes place. In order to achieve the same level of deformation, traditional FEM requires the performance of some re-meshing procedures, introducing a relevant source of errors. In addition, if the weight function is continuous together with its first *i*th derivatives, the derived global shape function is also continuous together with its first *i*th derivatives, see Belytschko et al. [6].

Also, since the global shape functions are constructed with the same intrinsic base, the approximation keeps the reproducibility property over the entire domain, an important MLSA characteristic. A sensitivity and convergence examination of the approximate solution with respect to the $\epsilon$ parameter is given in Alves and Rossi [2].

In order to impose the essential boundary condition, by directly prescribing the nodal values, one has to assure that no EFG weight functions do overlap any point at the boundary $\Gamma_u$. In order to achieve this goal, one considers:

(1) The partition of the domain into a triangular mesh so that each element defines an integration cell.
(2) The identification of the set of nodes of the mesh that belong to $\Gamma_u$ and the specification of an EPUFE weight function, centered at these nodes, constructed using a sufficiently small parameter $\epsilon$.
(3) The verification, at each of the remaining nodes of the integration mesh, if the trial EFG weight function centered at the given node, overlaps any point of the boundary $\Gamma_u$. If not, the trial EFG weight function is employed at the node. Otherwise, an EPUFE weight function is specified at the given node as done in (2).

Thus, each node of the integration mesh is assumed to be a center of a weight function and the shape of the support at the node depends whether one employs an EPUFE or an EFG weight function.

Notice that differently of the approach presented by Belytschko et al. [7], Krongauz and Belytschko [19], Hegen [13] and Huerta and Méndez [16] which combine mesh-free methods with FEM, this approach does not requires the partition of the domain into two different regions. Also, it is able to satisfy the linear consistency condition by simply employing the base, $\boldsymbol{p}^{\mathrm{T}}(\boldsymbol{X}) = [1, \boldsymbol{X}, \boldsymbol{Y}]$, over the entire domain. Moreover, it is important to notice that by using only EPUFE weight functions, the covering requirement is naturally satisfied. Thus, the covering strategy, defined in (7) and (8), is only necessary for the determination of the support of the EFG weight functions.

### 2.5.1 Covering algorithm

The strategy employed in the covering algorithm consists initially in a triangularization of the domain. Once the mesh nodes are defined one proceeds as follows:

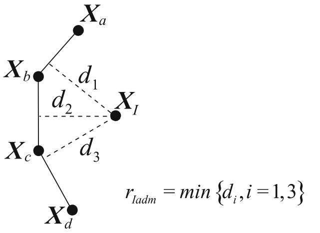

**Fig. 2** Definition of the admissible radius,$r_{\mathrm{Iadm}}$

```
• For each node $\boldsymbol{X}_I$ of the mesh, do:
  If ($\boldsymbol{X}_I \in \Gamma_u$) then
    Employ at $X_I$ an EPUFE weight, $w_I^{\mathrm{EPF}}(\boldsymbol{X})$.
  Else
    Determine the support of the trial EFG
    weight, $w_I^{\mathrm{EFG}}(\boldsymbol{X})$.
      (1) Get the set of adjacent nodes associated with node
      $\boldsymbol{X}_I$ (2) Determine the radius, $\bar{r}_I$ by (7),
      of the support of the trial EFG weight function
    Compute the admissible radius for the support, $r_{\mathrm{Iadm}}$, by
      determining the shortest distance from the given node
      $X_I$ to every boundary segment approximating $\Gamma_u$, as
      illustrated in Fig. 2.
    If ($\bar{r}_I < r_{\mathrm{Iadm}}$) then
      Employ at $\boldsymbol{X}_I$ the given trial EFG weight, $w_I^{\mathrm{EFG}}(\boldsymbol{X})$
    Else
      Employ at $\boldsymbol{X}_I$ an EPUFE weight, $w_I^{\mathrm{EPF}}(\boldsymbol{X})$
    End if
  End if
End do.
```

### 2.5.2 Transition from EFG to EPUFE shape functions

The aim of this section is to give some insight on the behavior of the shape functions in the neighborhood of the essential boundary $\Gamma_u$, which is fundamental for understanding the applicability and performance of the *F-bar* method, applied to cope with the volumetric locking phenomena, explained in Sect. 5.5.

Consider initially the particular case in which the base $\boldsymbol{p}^T(\boldsymbol{X}) = [1]$, the parameter $\varepsilon = 0$, and $\boldsymbol{X} \in \Omega_o$ is contained only in the interior of the support of PUFE weight functions. Then,

$$\mathbf{A}^{-1}(\boldsymbol{X}) = \frac{1}{\sum_{i=1}^{n} w(\boldsymbol{X} - \boldsymbol{X}_i)} \quad \text{and} \quad b_I = w(\boldsymbol{X} - \boldsymbol{X}_I).$$

Now, using the property that, $\sum_{i=1}^{n} w(\boldsymbol{X} - \boldsymbol{X}_i) = 1$, one derives

$$\Phi_I(\boldsymbol{X}) = \boldsymbol{p}^{\mathrm{T}}(\boldsymbol{X})[\mathrm{A}(\boldsymbol{X})]^{-1} b_I(\boldsymbol{X}) = w(\boldsymbol{X} - \boldsymbol{X}_I).$$

This result shows that, in this particular case, the computed shape function $\Phi_I(\boldsymbol{X})$ reproduces exactly the traditional FE interpolation functions, which in the scope of this work represents the conventional Tri3 finite element base function.

Now, consider the more general case where $\boldsymbol{p}^{\mathrm{T}}(\boldsymbol{X}) = [1, X, Y]$, $\varepsilon > 0$, and $\boldsymbol{X} \in \Omega_o$ is contained only in the interior of the support of EPUFE weight functions. In this case, as shown in Alves and Rossi [2, 34], the resulting shape function differs only slightly from the Tri 3 base function, which as seen in Sect. 6 will be responsible for a loss of efficiency of the *F-bar* method. The reason is that, in the FEM, the usage of Tri 3 elements results in a constant deformation gradient, $\mathbf{F} = \nabla_X \varphi(\boldsymbol{X}, t)$, making the mean dilatation approach, presented in Sect. 5.5, completely ineffective.

Now, let $\boldsymbol{X} \in \Omega_o$ be contained only in the interior of the support of EFG weight functions. In this case, the resulting approximating function may have an arbitrary degree of regularity, depending only on the regularity of the chosen weighting function, see Belytschko et al. [6], and is non-polynomial. This non-polynomial behavior is what suggests the applicability of the mean dilatation approach, which is investigated in Sect. 6. Notice that, in the FE framework, the applicability of the *F-bar* method requires the usage of high order interpolation functions, with special reduced quadrature rules, which increases the computational cost for solving large deformation problems.

## 3 Finite deformation

### 3.1 Kinematics of deformation

The model presented in this paper considers the multiplicative decomposition of the deformation gradient $\mathbf{F}$ into an elastic, $F^e$, and a plastic part, $\mathbf{F}^p$, as shown in Fig. 3, so

$$\mathbf{F} = \mathbf{F}^e \mathbf{F}^p, \tag{12}$$

where

$$\mathbf{F} = \nabla_X \varphi(\boldsymbol{X}, t). \tag{13}$$

Based on this assumption the rate of deformation can be decomposed additively as

$$\mathbf{D} = \mathbf{D}^e + \mathbf{D}^p. \tag{14}$$

The consideration of a $J_2$ plasticity model, which considers the plastic flow to be incompressible, implies that $\det(F^p) = 1$. Moreover, since $\det(\mathbf{F}) > 0$, one also obtain that $\det(F^e) > 0$.

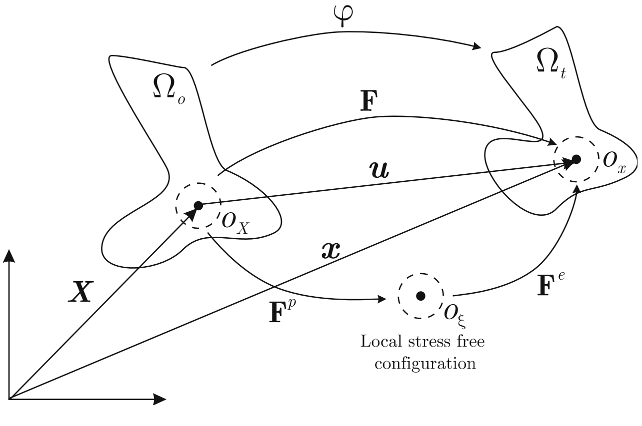

**Fig. 3** Multiplicative decomposition of the deformation gradient

Thus, the elastic deformation gradient admits a polar decomposition, i.e.,

$$\mathbf{F}^e = \mathbf{R}^{\mathrm{e}} \mathbf{U}^e, \tag{15}$$

where

$$\mathbf{U}^e = \sqrt{\mathbf{C}^{\mathrm{e}}} \tag{16}$$

with $\mathbf{C}^{\mathrm{e}}$ being the elastic right Cauchy–Green tensor given by

$$\mathbf{C}^e = \left(\mathbf{F}^e\right)^{\mathrm{T}} \mathbf{F}^e \tag{17}$$

and $\mathbf{R}^{\mathrm{e}}$ the elastic rotation tensor. The elastic deformation measure assumed in this work is the logarithmic or *Hencky* strain tensor, given by

$$\mathbf{E}^e = \ln\left(\mathbf{U}^e\right). \tag{18}$$

### 3.2 Conjugate stress measure

As pointed by Hill [14], in the formulation of constitutive theories, the stress–strain pairs must be such that the rate of work density remains preserved. As a result, the conjugate stress, associated with the *Hencky* strain, is the *rotated Kirchhoff* stress $\bar{\tau}$, given by

$$\bar{\tau} = \left(\mathbf{R}^{\mathrm{e}}\right)^{\mathrm{T}} \tau \mathbf{R}^{\mathrm{e}} \tag{19}$$

in which $\tau$ is the *Kirchhoff* stress, $\tau = \det(\mathbf{F})\sigma$, and $\sigma$ is the Cauchy stress.

### 3.3 Constitutive hyperelastic law, free energy and dissipation potentials

Here, one incorporates, to the $J_2$ plasticity model, a nonlinear isotropic hardening rule, described by the isotropic hardening strain $\alpha$. Moreover, in the framework of the thermodynamic of irreversible process, one assumes the existence of a free energy potential of the form:

$$\psi = \psi\left(\mathbf{E}^e, \alpha\right), \tag{20}$$

where

$$\rho_o \psi(\mathbf{E}^e, \alpha) = \tfrac{1}{2} \mathbb{D} \mathbf{E}^e \cdot \mathbf{E}^e + \tfrac{1}{2} H \alpha^2 + \left(\sigma_\infty - \sigma_y\right)\left[\alpha + \tfrac{1}{\delta} \mathrm{e}^{-\delta\alpha}\right]. \tag{21}$$

Here, $\rho_o$ is the mass density, $H$, $\delta$ and $\sigma_\infty$ are material parameters and $\sigma_{\mathrm{y}}$ is the initial yield stress. Moreover, $\mathbb{D}$ is the standard isotropic elasticity tensor, which is given by

$$\mathbb{D} = 2\mu \mathbb{I} + \left(\kappa - \frac{2}{3}\mu\right) \mathbf{I} \otimes \mathbf{I}, \tag{22}$$

where $\mathbb{I}$ and $\mathbf{I}$ are respectively the fourth order and the second order identities with $\mu$ and $\kappa$ denoting material parameters, known as shear and bulk modulus. The derived state equations are:

$$\bar{\tau} = \rho_o \frac{\partial \psi(\mathbf{E}^e, \alpha)}{\partial \mathbf{E}^e} = \mathbb{D} \mathbf{E}^e \tag{23}$$

for the rotated *Kirchhoff* stress and

$$k = \rho_o \frac{\partial \psi(\mathbf{E}^e, \alpha)}{\partial \alpha} = H\alpha + \left(\sigma_\infty - \sigma_y\right)\left(1 - \mathrm{e}^{-\delta\alpha}\right) \tag{24}$$

for the isotropic hardening stress $k$. This isotropic hardening relation was used by Simo and Armero [26], and also by Souza Neto et al. [29], where an investigation of the volumetric locking, in a large deformation process, was performed.

The dissipation associated with the elasto-plastic response is given by

$$D = \bar{\tau} \cdot \bar{\mathbf{D}}^p + k \cdot \dot{\alpha} \geq 0, \tag{25}$$

in which $\bar{\mathbf{D}}^p$ is the modified plastic stretching.

Here, one considers the yield function to be given by

$$\mathcal{F}(\bar{\tau},k) = \sqrt{3J_2} - \left[k(\alpha) + \sigma_y\right] \tag{26}$$

where

$$J_2 = \frac{1}{2}\bar{\tau}^D \cdot \bar{\tau}^D \tag{27}$$

and

$$\bar{\tau}^D = \bar{\tau} - \frac{1}{3}tr(\bar{\tau})\mathbf{I}. \tag{28}$$

Hence, the admissible stress state $\mathcal{E}$ is defined as

$$\mathcal{E} = \{\, \bar{\tau} \mid \mathcal{F}(\bar{\tau}, k) \leq 0\}. \tag{29}$$

In order to describe the dissipative elasto-plastic process, one needs to introduce complementary kinetic laws. These kinetic laws are obtained by the introduction of a pseudo-potential of dissipation and by the application of the normal dissipation hypothesis. Now, since the $J_2$ plasticity model is associative, one derives, from the normal dissipation hypothesis, the following evolution equations:

- The plastic flow equation

$$\bar{\mathbf{D}}^p = \dot{\lambda}\frac{\partial \mathcal{F}}{\partial \bar{\tau}}. \tag{30}$$

- The isotropic hardening evolution

$$\dot{\alpha} = -\dot{\lambda}\frac{\partial \mathcal{F}}{\partial k}. \tag{31}$$

Here, $\lambda$ is the plastic multiplier and must satisfy the following complementary conditions

$$\mathcal{F} \leq 0, \;\; \dot{\lambda} \geq 0 \text{ and } \dot{\lambda}\mathcal{F} = 0. \tag{32}$$

## 4 The elasto-plastic initial value problem

The elasto-plastic problem presented in Sect. 3 is dependent on the deformation history. Thus, in order to integrate the evolution equations from time step $t_n$ to $t_{n+1}$, one must solve an initial value problem. The elasto-plastic constitutive initial value problem can be stated as: Given the deformation history $\mathbf{F}(t), \; t \in [t_n, t_{n+1}]$ and the initial conditions

$$\begin{aligned} &\mathbf{F}^p(t_n) = \mathbf{F}_n^p \\ &\alpha(t_n) = \alpha_n \end{aligned} \tag{33}$$

determine $\mathbf{F}_{n+1}^p$ and $\alpha_{n+1}$ such that the (23), (30), (31) and (32) are satisfied.

With the aim of solving the elasto-plastic initial value problem one applies the operator split method. Thus, the nonlinear evolution problem is split into a sequence of two sub problems that are:

- the elastic predictor problem;
- the plastic corrector problem.

### 4.1 The elastic predictor problem

In this step, the material is assumed to behave purely hyper elastically between times $t_n$ to $t_{n+1}$. Hence, the elastic predictor problem may be stated as: Given the initial conditions $\mathbf{F}^p(t_n) = \mathbf{F}_n^p$ and $\alpha(t_n) = \alpha_n$ together with the history of the deformation gradient $\mathbf{F}(t), \; t \in [t_n, t_{n+1}]$. Then, the initial value problem consists in finding $F^p(t)$ and $\alpha(t)$ so that

$$\dot{\mathbf{F}}^p = 0 \tag{34}$$

and

$$\dot{\alpha} = 0 \tag{35}$$

for $t \in \left[t_n, t_{n+1}\right]$. The solution to the elastic predictor problem at time $t_{n+1}$, defining the so called elastic trial state, is given by

$$\mathbf{F}_{n+1}^{p^{\text{trial}}} = \mathbf{F}_n^p, \quad \alpha_{n+1}^{\text{trial}} = \alpha_n, \tag{36}$$

$$\mathbf{F}_{n+1}^{e^{\text{trial}}} = \mathbf{F}_{n+1}\left(\mathbf{F}_n^p\right)^{-1}, \quad \mathbf{C}_{n+1}^{e^{\text{trial}}} = \left(\mathbf{F}_{n+1}^{e^{\text{trial}}}\right)^T \mathbf{F}_{n+1}^{e^{\text{trial}}},$$

$$\mathbf{E}_{n+1}^{e^{\text{trial}}} = \frac{1}{2}\ln\left(\mathbf{C}_{n+1}^{e^{\text{trial}}}\right), \bar{\tau}_{n+1}^{\text{trial}} = \mathbb{D}\mathbf{E}_{n+1}^{e^{\text{trial}}} \quad \text{and} \quad k_{n+1}^{\text{trial}} = k_n.$$

### 4.2 The plastic corrector problem

The plastic corrector step is only solved whenever $\bar{\tau}_{n+1}^{\text{trial}} \notin \bar{\mathcal{E}}$, i.e., the trial elastic state is not feasible, what corresponds to $\mathcal{F}\left(\bar{\tau}_{n+1}^{\text{trial}}, k_{n+1}^{\text{trial}}\right) > 0$. This step considers a return mapping algorithm that incorporates: a backward exponential approximation to the plastic flow equation (see Eterovic and Bathe [10] and Weber and Anand [32]), a fully implicit standard Euler backward approximation to the hardening evolution and the enforcement of the yield criterion. The initial conditions, for this step, are given by the trial elastic state.

Now, based on the above considerations, the plastic flow equation

$$\mathbf{F}^p = \bar{\mathbf{D}}^p\mathbf{F}^p \tag{37}$$

is discretized, based on the backward exponential approximation, as

$$\mathbf{F}_{n+1}^p = \exp\left(\bar{\mathbf{D}}_{n+1}^p\right)\mathbf{F}_n^p. \tag{38}$$

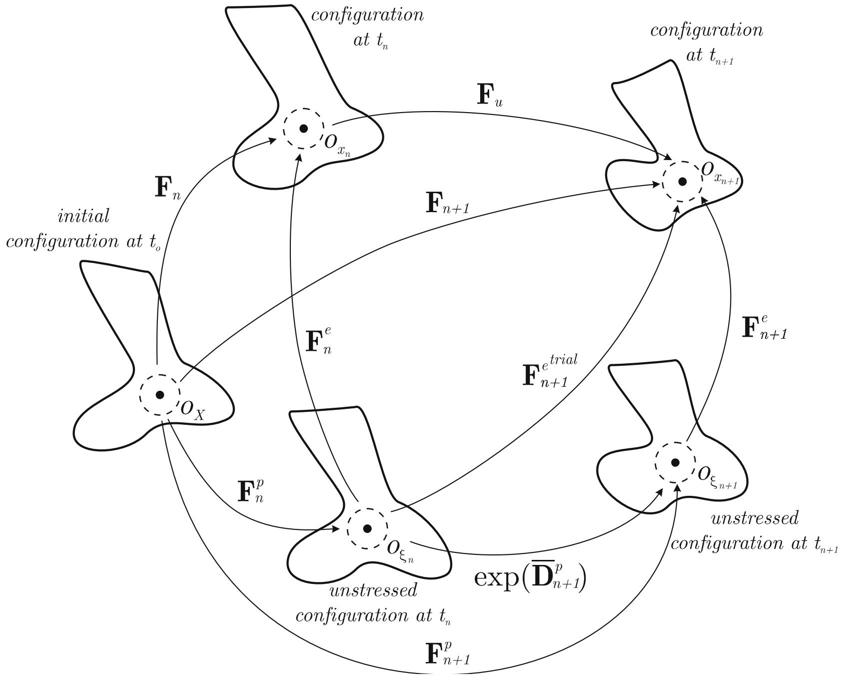

**Fig. 4** Kinematics of deformation in the presented algorithm

Moreover, after a straightforward manipulation, (39) reduces to

$$\mathbf{E}^e_{n+1} = \mathbf{E}^{e^{\text{trial}}}_{n+1} - \Delta\lambda \mathbf{N}_{n+1} \tag{39}$$

with

$$\mathbf{N}_{n+1} = \left.\frac{\partial \mathcal{F}}{\partial \bar{\tau}}\right|_{n+1} \tag{40}$$

and

$$\bar{\mathbf{D}}^p_{n+1} = \Delta\lambda \mathbf{N}_{n+1}. \tag{41}$$

Also, it can be shown that

$$\mathbf{R}^e_{n+1} = \mathbf{R}^{e^{\text{trial}}}_{n+1}. \tag{42}$$

The isotropic hardening evolution law

$$\dot{\alpha} = \dot{\lambda} \tag{43}$$

is discretized by the fully implicit Euler backward method, resulting in

$$\alpha_{n+1} - \alpha_n - \Delta\lambda = 0. \tag{44}$$

As a result, the plastic corrector scheme reduces to the solution of the following set of nonlinear equations, for $\mathbf{E}^e_{n+1}$, $\alpha_{n+1}$ and $\Delta\lambda$, with

$$\begin{cases} \mathbf{E}^e_{n+1} - \mathbf{E}^{e^{\text{trial}}}_{n+1} + \Delta\lambda \mathbf{N}_{n+1} \\ \alpha_{n+1} - \alpha_n - \Delta\lambda \\ \mathcal{F}(\bar{\tau}_{n+1}, k(\alpha_{n+1})) \end{cases} = \begin{bmatrix} 0 \\ 0 \\ 0 \end{bmatrix}. \tag{45}$$

Figure 4 sketches the deformation process in the algorithm.

## 5 A total Lagrangean formulation

### 5.1 Strong formulation of the problem

The finite deformation elasto-plastic problem may be stated as: determine $\boldsymbol{u}$ so that

$$\begin{aligned} div\,\mathbf{P} + \rho_o \bar{\boldsymbol{b}} &= 0 \quad \text{in}\,\Omega_o \\ \mathbf{P}\boldsymbol{m} &= \bar{\boldsymbol{t}} \quad \text{in}\,\Gamma_t\ , \\ \boldsymbol{u} &= \bar{\boldsymbol{u}} \quad \text{in}\,\Gamma_u \end{aligned} \tag{46}$$

where $\mathbf{P}$ is the first *Piola–Kirchhoff* stress, $\boldsymbol{m}$ is the outer normal on $\partial\Omega_o$ and $\bar{\boldsymbol{b}}$, $\bar{\boldsymbol{t}}$ and $\bar{\boldsymbol{u}}$ are the prescribed body force, traction vector and displacement field respectively.

### 5.2 Weak formulation of the problem

Let $H = \left\{\boldsymbol{u} |\ u_i \in W^1_p(\Omega_o),\ \boldsymbol{u}{=}\bar{\boldsymbol{u}}\ on\ \Gamma_u\right\}$ denote the set of admissible displacements and $H_o = \{\boldsymbol{u} \in H |\ \ \boldsymbol{u}{=}\ 0\ on\ \Gamma_u\}$ the set of admissible variations. The weak formulation of the problem may be stated as: find $\boldsymbol{u}_{n+1} \in H$ such that

$$\mathcal{G}\big(\boldsymbol{u}_{n+1}, \hat{\boldsymbol{u}}\big) = 0 \quad \forall\, \hat{\boldsymbol{u}} \in H_o \tag{47}$$

where

$$\begin{aligned} \mathcal{G}\big(\boldsymbol{u}_{n+1}, \hat{\boldsymbol{u}}\big) = &\int_{\Omega_o} \mathbf{P}(\boldsymbol{u}_{n+1}) \cdot \nabla_X \hat{\boldsymbol{u}}\ \mathrm{d}\Omega_o \\ &- \int_{\Omega_o} \rho_o \bar{\boldsymbol{b}} \cdot \hat{\boldsymbol{u}}\, \mathrm{d}\Omega_o - \int_{\Gamma_{o_t}} \bar{\boldsymbol{t}} \cdot \hat{\boldsymbol{u}}\ \mathrm{d}\Gamma_{o_t}. \end{aligned} \tag{48}$$

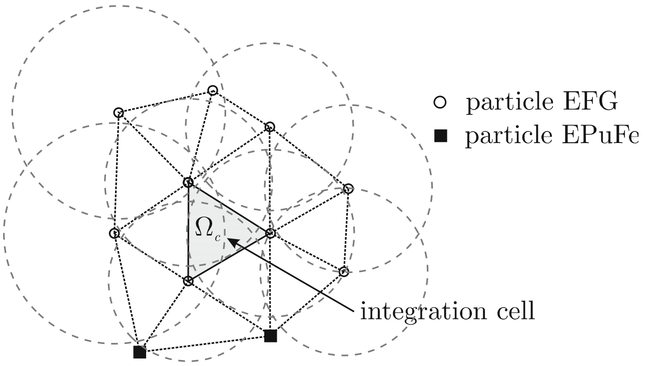

**Fig. 5** Definition of the integration cell

### 5.3 Linearization and Newton method

The solution of the nonlinear problem in (48) is obtained by applying *Newton's* method. In this context the linearization of the functional $\mathcal{G}\big(\boldsymbol{u}_{n+1}, \hat{\boldsymbol{u}}\big)$ is required. Assuming $\mathcal{G}$ to be sufficiently regular and that

$$\mathcal{G}\left(\boldsymbol{u}_{n+1}^{k+1}, \hat{\boldsymbol{u}}\right) = \mathcal{G}\left(\boldsymbol{u}_{n+1}^{k} + \Delta\boldsymbol{u}_{n+1}^{k}, \hat{\boldsymbol{u}}\right) = 0, \tag{49}$$

one derives

$$\begin{aligned}\mathcal{G}\big(\boldsymbol{u}_{n+1}^{k} + \Delta\boldsymbol{u}_{n+1}^{k}, \hat{\boldsymbol{u}}\big) &= \mathcal{G}\big(\boldsymbol{u}_{n+1}^{k}, \hat{\boldsymbol{u}}\big)\\ &+ D\mathcal{G}\big(\boldsymbol{u}_{n+1}^{k}, \hat{\boldsymbol{u}}\big)\big[\Delta\boldsymbol{u}_{n+1}^{k}\big]\end{aligned} \tag{50}$$

where

$$\begin{aligned}D\mathcal{G}\left(\boldsymbol{u}_{n+1}^{k}, \hat{\boldsymbol{u}}\right)\left[\Delta\boldsymbol{u}_{n+1}^{k}\right] &= \left.\frac{\mathrm{d}}{\mathrm{d}\varepsilon}\right|_{\varepsilon=0} \mathcal{G}\left(\boldsymbol{u}_{n+1}^{k} + \varepsilon\Delta\boldsymbol{u}_{n+1}^{k}, \hat{\boldsymbol{u}}\right)\\ &= \int\limits_{\Omega_o} \mathbb{A}(\boldsymbol{u}_{n+1}) \cdot \nabla_X\left(\Delta\boldsymbol{u}_{n+1}^{k}\right) \cdot \nabla_X\hat{\boldsymbol{u}}\ \mathrm{d}\Omega_o\end{aligned} \tag{51}$$

with

$$\begin{aligned}[\mathbb{A}]_{ijkl} &= \frac{\partial P_{ij}}{\partial F_{kl}}\\ &= \frac{\partial \tau_{ip}}{\partial F_{kl}} F_{jp}^{-1} - \tau_{ip} F_{jk}^{-1} F_{lp}^{-1}.\end{aligned} \tag{52}$$

### 5.4 Determination of $\mathbb{A}$

Now, the determination of $\mathbb{A}$ requires the derivative of the *Kirchhoff* stress tensor with respect to the deformation gradient. As already seem, the *Kirchhoff* stress is related to the rotated *Kirchhoff* stress by (19). This means that in the determination of (53) a derivative of the rotated *Kirchhoff* stress with respect to the deformation gradient takes place. But since

$$\bar{\tau}_{n+1} = \hat{\bar{\tau}}_{n+1}\left(\mathbf{E}_{n+1}^{e^{\text{trial}}}, (\bullet)_n\right), \tag{53}$$

one may use the chain rule of differentiation to derive

$$\hat{\mathbb{D}} = \frac{\partial \bar{\tau}_{n+1}}{\partial \mathbf{F}_{n+1}} = \frac{\partial \bar{\tau}_{n+1}}{\partial \mathbf{E}_{n+1}^{e^{\text{trial}}}} \frac{\partial \mathbf{E}_{n+1}^{e^{\text{trial}}}}{\partial \mathbf{C}_{n+1}^{e^{\text{trial}}}} \frac{\partial \mathbf{C}_{n+1}^{e^{\text{trial}}}}{\partial \mathbf{F}_{n+1}} = \tilde{\mathbb{D}}\mathbb{G}\mathbb{H}, \tag{54}$$

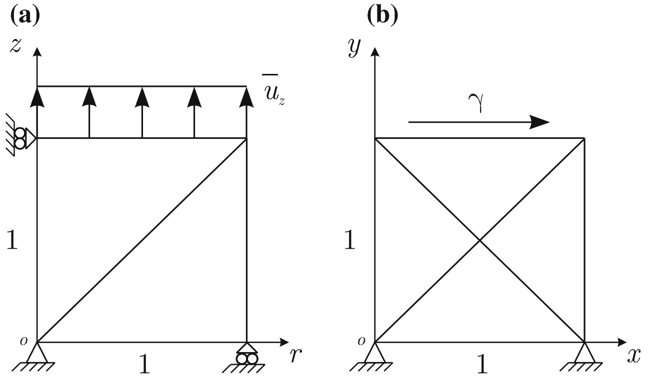

**Fig. 6** **a** One-dimensional axisymmetric model and **b** simple shear model

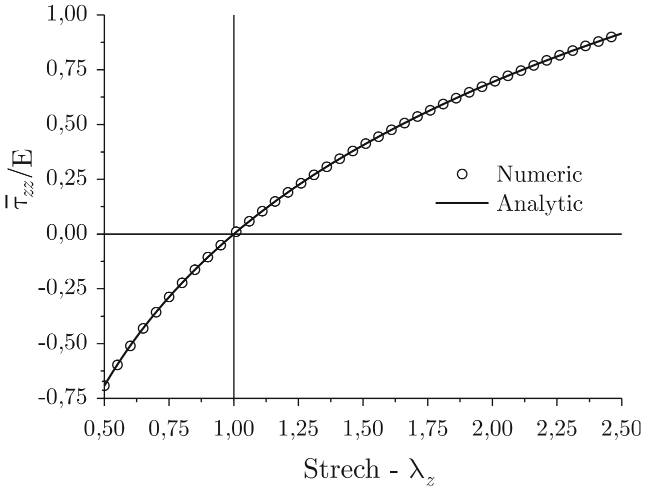

**Fig. 7** Analytic versus numeric results for simple tension-compression test

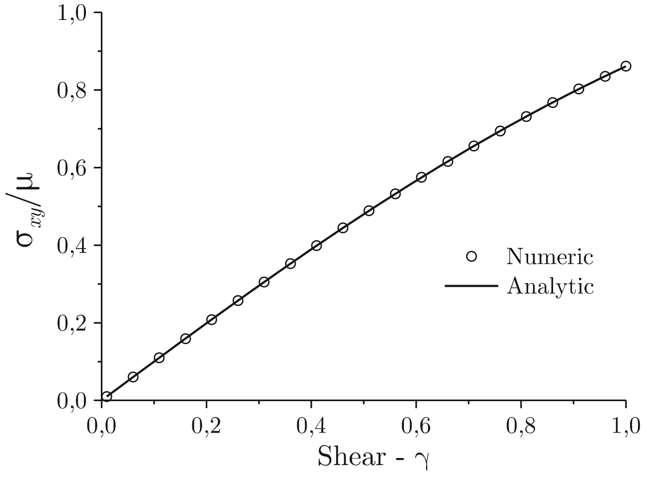

**Fig. 8** Analytic versus numeric results for pure shear simulation

where

$$\tilde{\mathbb{D}} = \frac{\partial \bar{\tau}_{n+1}}{\partial \mathbf{E}_{n+1}^{e^{\text{trial}}}}, \tag{55}$$

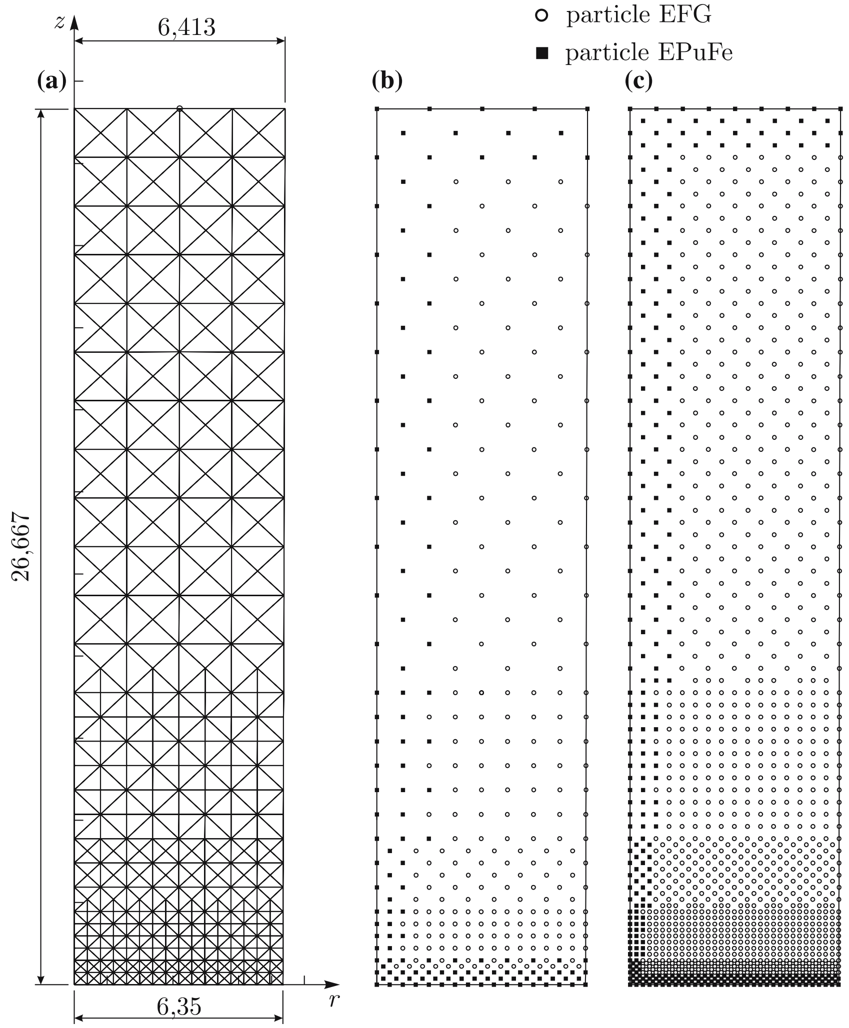

**Fig. 9** Integration meshes **a** FEM – 1379 nodes, **b** MEFG – 364 nodes and **c** MEFG – 1379 nodes

$$\mathbb{G} = \frac{\partial \mathbf{E}^{e^{\text{trial}}}_{n+1}}{\partial \mathbf{C}^{e^{\text{trial}}}_{n+1}}, \tag{56}$$

and

$$\mathbb{H} = \frac{\partial \mathbf{C}^{e^{\text{trial}}}_{n+1}}{\partial \mathbf{F}_{n+1}}. \tag{57}$$

The terms $\mathbb{G}$ and $\mathbb{H}$ in (55) are related with the geometric part of $\hat{\mathbb{D}}$ and are given by

$$[\mathbb{H}]_{ijkl} = \frac{\partial C^{e^{\text{trial}}}_{n+1_{ij}}}{\partial F_{n+1_{kl}}} = F^{p^{-1}}_{n_{li}} F^{e^{\text{trial}}}_{n+1_{kj}} + F^{e^{\text{trial}}}_{n+1_{ki}} F^{p^{-1}}_{n_{lj}} \tag{58}$$

and

$$\begin{aligned} \mathbb{G} &= \frac{\partial \mathbf{E}^{e^{\text{trial}}}_{n+1}}{\partial \mathbf{C}^{e^{\text{trial}}}_{n+1}} = \frac{\partial}{\partial \mathbf{C}^{e^{\text{trial}}}_{n+1}} \ln\left(\mathbf{U}^{e^{\text{trial}}}_{n+1}\right) \\ &= \frac{1}{2} \frac{\partial}{\partial \mathbf{C}^{e^{\text{trial}}}_{n+1}} \ln\left(\mathbf{C}^{e^{\text{trial}}}_{n+1}\right). \end{aligned} \tag{59}$$

Notice that in the (60) a derivative of the type $\frac{\partial}{\partial \mathbf{X}}\ln(\mathbf{X})$ is required, which consists of a derivative of an isotropic tensor function, which was investigated in details in Ortiz et al. [22]. Moreover, $\tilde{\mathbb{D}}$ is the only contribution related to the constitutive relation in the consistent tangent modulus$\mathbb{A}$. Its determination depends if the state is elastic, $\mathcal{F} \leq 0$, or elasto-plastic $\mathcal{F} > 0$. Then

$$\tilde{\mathbb{D}} = \begin{cases} \mathbb{D} & if\ \mathcal{F} \leq 0 \\ \mathbb{D}^{ep} & if\ \mathcal{F} > 0 \end{cases}. \tag{60}$$

Here, $\mathbb{D}$ is the elasticity tensor given in (22) and $\mathbb{D}^{ep}$ is the elasto-plastic modulus that must be identified for each given constitutive model. For the $J_2$-plasticity model presented in this paper

$$\begin{aligned} \mathbb{D}^{\text{ep}} &= \frac{\mathrm{d}\bar{\tau}_{n+1}}{\mathrm{d}\mathbf{E}^{e^{\text{trial}}}_{n+1}} \\ &= \left(\mathbb{D}^{-1} + \Delta\lambda \frac{\partial \mathbf{N}_{n+1}}{\partial \bar{\mathbf{T}}_{n+1}} - \frac{1}{\partial \mathcal{F}/\partial \alpha_{n+1}} \mathbf{N}_{n+1} \otimes \mathbf{N}_{n+1}\right)^{-1}. \end{aligned} \tag{61}$$

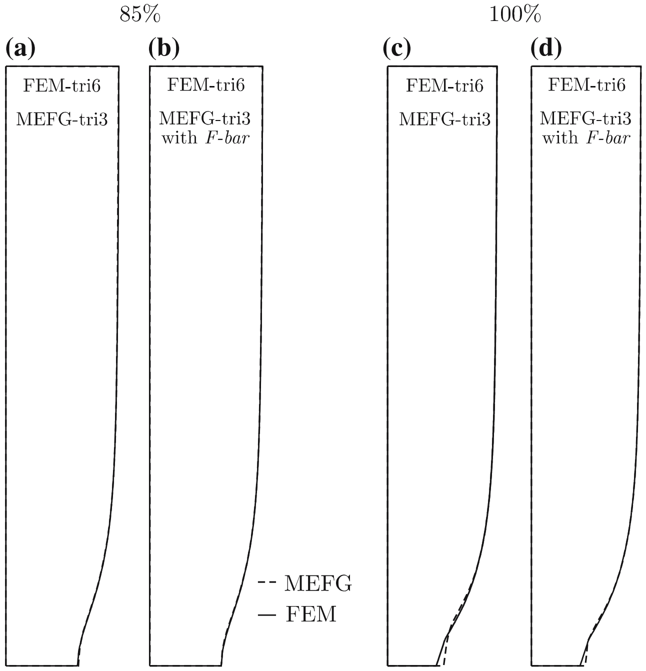

**Fig. 10** Comparison among deformed bodies at 85% and 100% of the process

### 5.5 An F-bar implementation

Basically, the *F-bar* methodology requires that the deformation gradient be decomposed into a volumetric and an deviatoric component

$$\mathbf{F} = \mathbf{F}_{\text{dev}}\mathbf{F}_{\text{vol}} \tag{62}$$

with

$$\mathbf{F}_{\text{dev}} = [\det(\mathbf{F})]^{-\frac{1}{3}}\mathbf{F} \tag{63}$$

and

$$\mathbf{F}_{\text{vol}} = [\det(\mathbf{F})]^{\frac{1}{3}}\mathbf{I}. \tag{64}$$

The basic *F-bar* methodology considers $\mathbf{F}_{\text{vol}}$ to be computed as a constant term within each finite element. Thus,

$$\bar{\mathbf{F}} = \mathbf{F}_{\text{dev}}(\mathbf{F}_a)_{\text{vol}} = \left(\frac{\det(\mathbf{F}_a)}{\det(\mathbf{F})}\right)^{\frac{1}{3}}\mathbf{F}. \tag{65}$$

Souza Neto et al. [28] promotes that this constant term be calculated by the interpolation of $\mathbf{F}$ at the baricenter of the integration cell $\Omega_c$, see Fig. 5. Here one considers the average term $\det(\mathbf{F}_a)$ to be computed as

$$\det(\mathbf{F}_a) = \frac{1}{\Omega_c}\int_{\Omega_c}\det(\mathbf{F})\,\mathrm{d}\Omega_c, \tag{66}$$

which is known as the *mean dilatation* procedure. This is a well established procedure used to prevent volumetric locking in FEM and its extension to the mesh-free methods can be performed in a natural way once the integration cell is defined. However, the numerical integration requirement in (67) introduces a completely different perspective inside the EFG. As in the integration of the weak form, (67) also requires the information of the support of each integration point. Thus, the average $\det(\mathbf{F}_a)$ will depend strongly on the shape function form. In the particular case of the MEFG method, at cells covered only by EPuFE shape functions, since the EPuFE shape functions differ only slightly from the classical Tri3 finite element base functions, the resulting deformation gradient, $\mathbf{F}$, will be approximately constant in cell, making the anti-volumetric locking strategy completely ineffective over this area (see Alves and Rossi [3, 25]).

The derivation of the internal force in (48) and the tangent stiffness in (53) is achieved by making the following composition

$$\mathbf{P} = \mathbf{P} \circ \phi(\mathbf{F}) \tag{67}$$

with $\phi(\mathbf{F}) = \bar{\mathbf{F}}$. Thus,

$$\begin{aligned} \left[\bar{\mathbb{A}}\right]_{ijkl} &= \frac{\partial P_{ij}}{\times}\partial \bar{F}_{rs}\frac{\partial \bar{F}_{rs}}{\times}\partial F_{kl}. \\ \left[\bar{\mathbb{A}}\right]_{ijkl} &= \frac{\partial P_{ij}}{\partial \bar{F}_{rs}}\partial \bar{F}_{rs}\frac{\partial \bar{F}_{rs}}{\partial F_{kl}} \end{aligned} \tag{68}$$

At this point, it is important to notice that Akkaram and Zabaras [1] had observed some hour-glass instabilities in the deformation pattern for the *F-bar* approach, when applied in the scope of the finite element method, and have devised a stabilization procedure of the form

$$\bar{\mathbf{F}}_{\text{new}} = (1-\beta)\bar{\mathbf{F}} + \beta\mathbf{F}, \tag{69}$$

where $\bar{\mathbf{F}}_{\text{new}}$ is the value actually implemented, due to the modified *F-bar* approach, and $\beta$ is an empirical small positive parameter, $\beta \to 0$. Also, in the context of the FEM, the *F-bar* method can only be applied to elements with a high order of interpolation, i.e. it's not applicable to tri3 elements.

Here, due to the non-polynomial nature of the EFG global base functions, the *F-bar* method may be applied to a tri3 type of particle distribution. Moreover, no hour-glass instability problems have been observed so far in the examples solved in this work.

## 6 Examples

In order to validate the proposed procedure, some problem cases are numerically investigated. These examples were selected among the ones found in the literature, used for evaluation of the volumetric locking phenomenon. The solution to these problems allow the comparison of the MEFG results, obtained with the proposed *F-bar* approach, with the results presented in other papers.

Unless stated contrary, the parameters used in (7) and (10) are set as: $s = 1.5$ and $\varepsilon = 10^{-4}$.

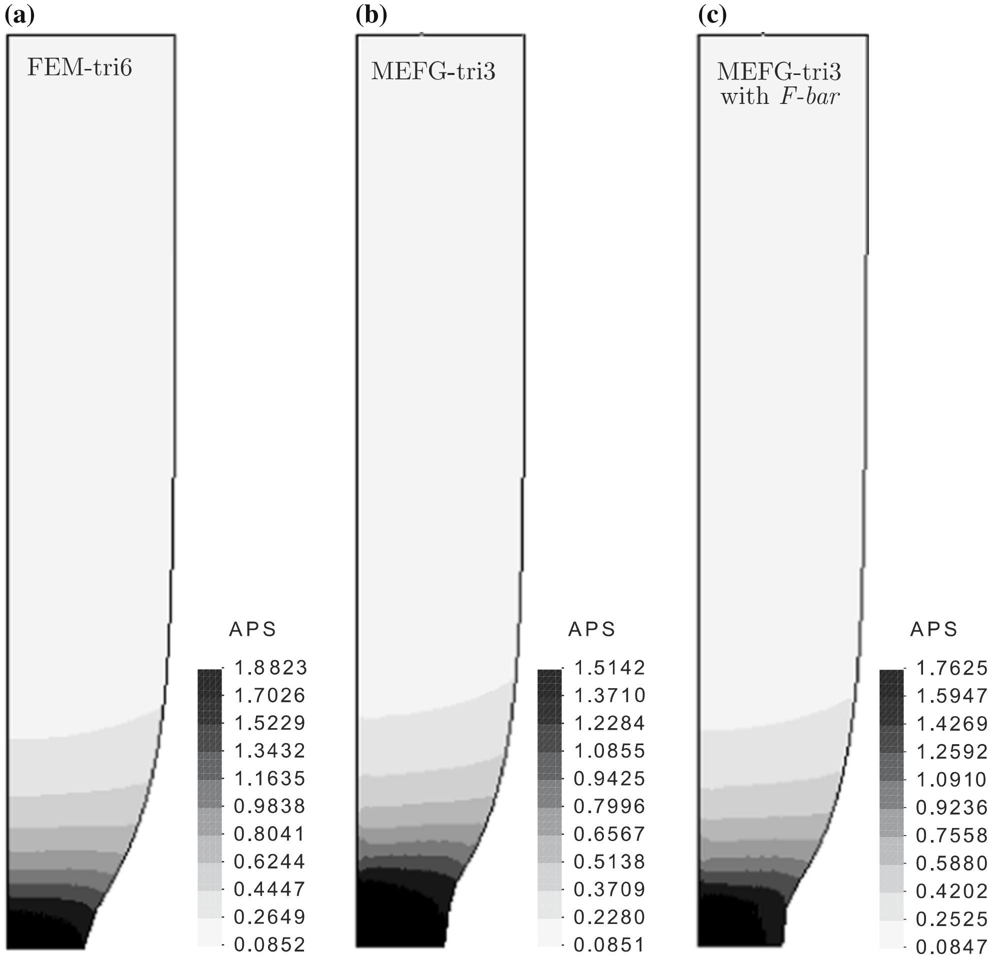

**Fig. 11** Accumulated plastic strain at the end of the process

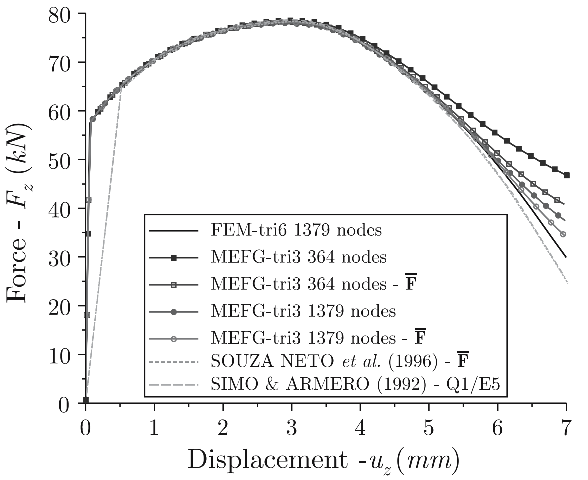

**Fig. 12** Comparison between force versus displacement at the top of the body

### 6.1 Simple tension-compression and pure shear: hyperelastic deformation tests

A simple tension-compression analysis is carried out in order to illustrate the nonlinear constitutive relation among the rotated *Kirchhoff* stress and the logarithmic deformation. Considering a one-dimensional model, as illustrated in Fig. 6a, it can be shown that

$$\bar{\tau}_{zz} = E \ln(\lambda_z) \tag{70}$$

with

$$E = \frac{9\kappa\mu}{3\kappa + \mu}, \tag{71}$$

where $\lambda_z$ is the stretching on the $z$ direction. The material parameters adopted for this analysis are: $\kappa = 164206.35\,\text{MPa}$ and $\mu = 80193.80\,\text{MPa}$.

Figure 7 compares the analytical and the numerical solutions for this problem case. It is also plotted the normalized stress $(\bar{\tau}_{zz}/E)$ versus the stretch $\lambda_z$.

Figure 8 depicts the results determined in the pure shear case, which is illustrated in Fig. 6b, where the plane strain hypothesis is assumed. Analytic results in terms of the Cauchy stress for this problem case are available in the literature, see Weber and Anand [32], and are given as

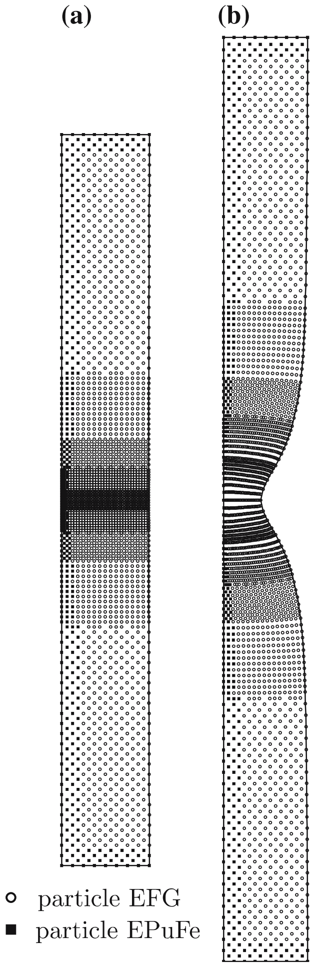

**Fig. 13** **a** undeformed model **b** deformed configuration

$$\sigma_{xx} = \sigma_{yy} = \frac{1}{2}\gamma\sigma_{xy}$$
$$\sigma_{xy} = \mu\gamma\left[\frac{1}{\gamma\sqrt{1+\frac{1}{4}\gamma^2}}\ln\left(1+\frac{1}{2}\gamma^2+\gamma\sqrt{1+\frac{1}{4}\gamma^2}\right)\right]. \tag{72}$$

Figure 8 plots the normalized Cauchy shear stress $\sigma_{xy}/\mu$ versus the shear strain $\gamma$, obtained both numerically and analytically, for a comparison purpose. Here, again, one sees a fine agreement between the results.

## 6.2 Necking of a circular bar

Here, one considers the analysis of a hypothetical cylindrical bar with the objective of verifying the necking behavior. The model of the problem, illustrated in Fig. 9, consists of a bar with a length of 53.334 mm and a radius of 6.413 mm. Due to the symmetry condition, only a quarter of the model is discretized. The model is submitted to a prescribed displacement, $u_z = 7$ mm, in the upper surface of the bar. The prescribed displacement is applied by a linear ramp where several steps are considered. To trigger the necking, a small geometric imperfection is introduced into the model. This imperfection consists of a variation of the radius in the central

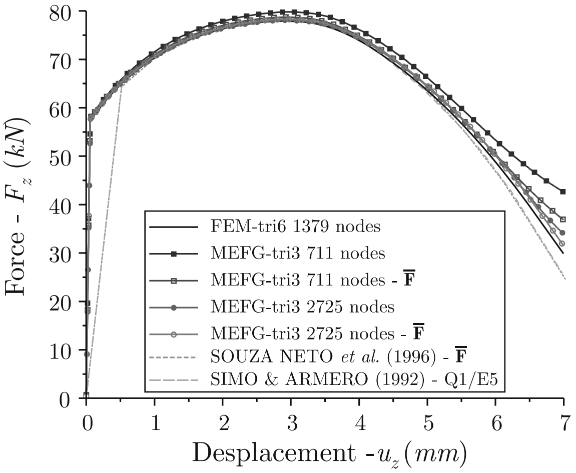

**Fig. 14** Comparison between force versus displacement at the top of the body

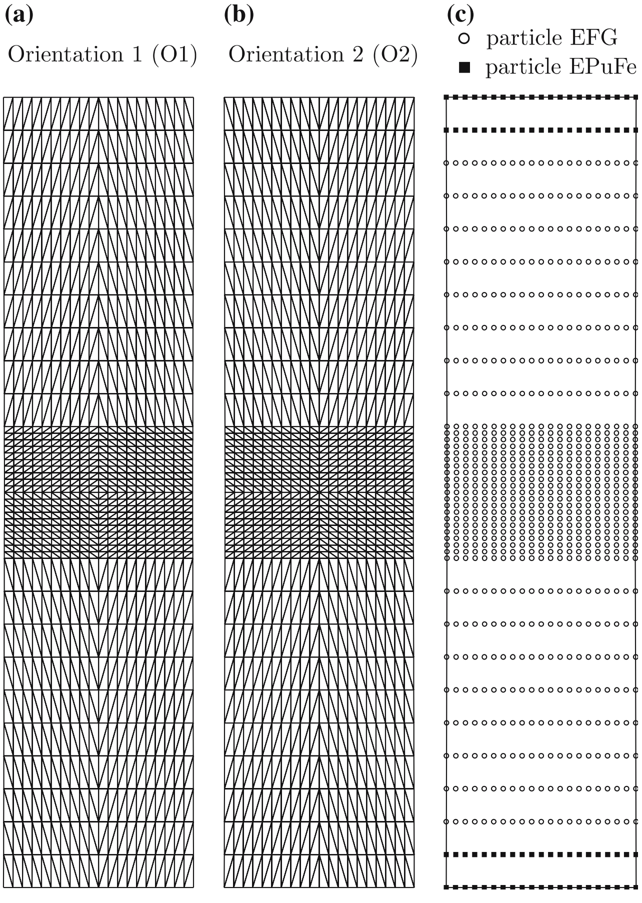

**Fig. 15** Integration meshes and particle distribution used in the plane strain example

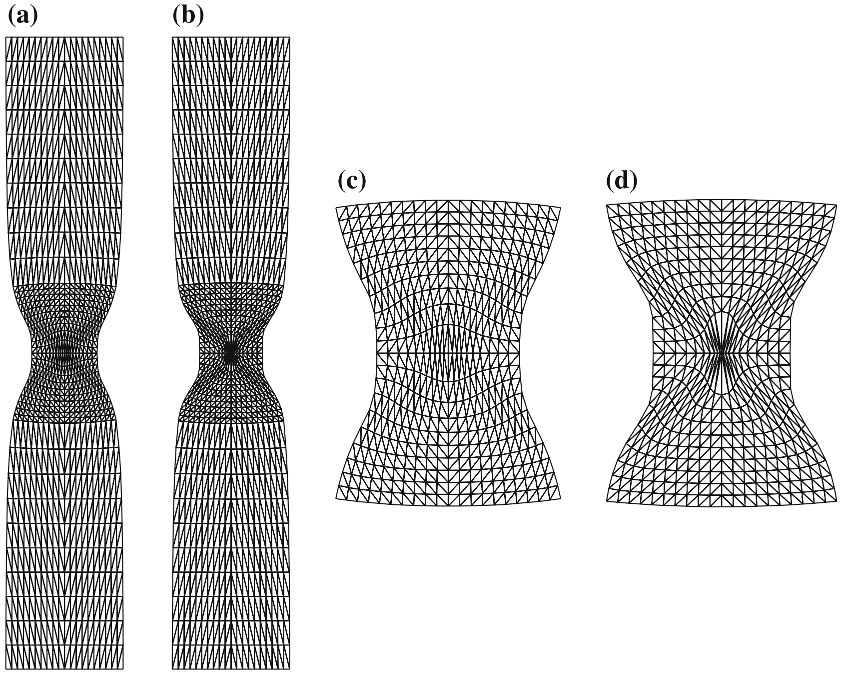

**Fig. 16** Deformed configurationsFEM-tri6

region of 1%, i.e., the radius of the central region is 6.35 mm. Similar examples are presented in the works of Simo and Armero [26] and Souza Neto et al. [28] where an investigation of the volumetric locking problem was accomplished. Fig. 9a shows the discretization of the domain into triangular integration cells. The mesh presented in Figure 9a is also used in a finite element simulation, employing a classical tri6 element, with a mesh of 1379 nodes. Figure 9b, c shows the MEFG particle distribution that contains 364 and 1379 nodes/particles, respectively. The material properties used are: $\kappa$ = 164206.35 MPa, $\mu$ = 80193.80 MPa, $H$ = 129.24 MPa, $\delta$ = 16.93, $\sigma_\infty = 715$ MPa and $\sigma_y = 450$ MPa.

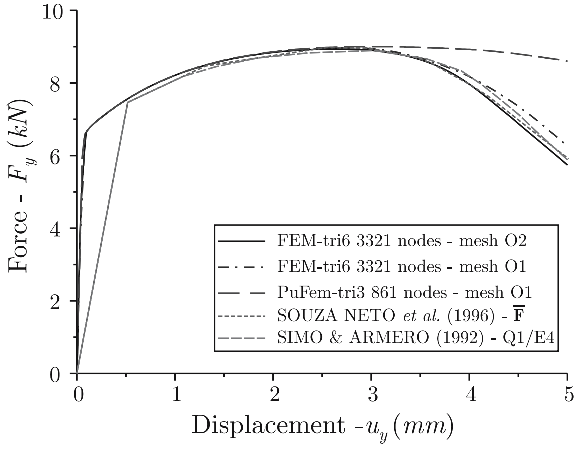

**Fig. 17** Force versus displacement at the top of the body, FEM-tri6

Figure 10 shows the comparisons among the deformed configurations of the body outline at 85 and 100% of the total prescribed displacement, considering the meshes in Figure 9a, c with and without the *F-bar* methodology. Note that at 85 there is no apparent distinction between the two methods. However, at 100% of the process, a discrepant difference is verified in the necking region. Note also that there is a relevant difference, in the necking region, when the *F-bar* methodology is considered.

Differences are also noted when the accumulated plastic strain analysis, shown in Fig. 11, is considered, where the results were obtained for the meshes in Figure 9a, c.

Figure 12 plots the force *versus* displacement diagram calculated at the top of the bar. It is clear from this figure that the results remain close to one another during a great part of the deformation process. In a certain threshold point, looking what seems to be an inflection point, the solution moves away from that achieved using the finite element method. Notice again that the implementation of the *F-bar* procedure generates improved results when compared with the finite element solution. Also is plotted, in this figure, the results presented by Simo and Armero [26] and Souza Neto et al. [28].

### *6.2.1 Half simetry*

In the previous example, where a quarter of symmetry was imposed, the region with the highest deformation level was precisely the one which was covered by EPuFe weight functions, due to the enforcement of the two symmetry conditions. Notice that, as commented in Alves and Rossi [2], when only

EPuFe weight functions are used for the EFG approximation, the resulting global base functions tend to reproduce the standard tri3 finite element type of base function, what causes a deterioration of the approximate solution, making it prone to the volumetric locking phenomenon.

In order to allow the contribution of spline weight functions in the central region, a model that enforces only a half symmetry condition is considered, as illustrated in Fig. 13a. Figure 13b shows the deformed configuration at the end of the deformation process.

The results in terms of force *versus* displacement are presented in Fig. 14. Again, the force and the displacement are "measured" on the top of the structure. Notice that the MEFG results for this example are closer to those obtained considering the FEM, using a Tri6 element. Again, the results presented by Simo and Armero [26] and Souza Neto et al. [28] are also plotted in Fig. 14.

### 6.3 Plane strain localization and mesh dependency

In this example, a uniaxial traction model of a rectangular bar under plane strain condition is presented. The dimensions of the bar coincide with those presented in the previous examples. That is, instead of having a radius of 6.413 mm it will have a dimension defining one half of the base of the rectangular bar. Again, a small geometric imperfection is introduced in the model. This imperfection consists of a variation in the central region of the 1% model, which is the distance from the center of the rectangular bar to the lateral is 6.35 mm. This bar is then submitted to a prescribed displacement of $u_z = 5$ mm in both the extremities.

In order to prevent a loss of regularity, when using EPuFe particles, the entire domain was discretized.

The material parameters are the same as the ones used in the previous example, with the exception of the parameter $H$ employed in the hardening rule, which is assumed to be: $H = -12.924$ MPa, as suggested by Simo and Armero [26].

This example verifies if the solution of the problem suffers from a integration mesh dependency. Therefore, two integration meshes with the same distribution and number of particles, 861, but with different orientations of the integration cells are proposed. These integration meshes are shown in Fig. 15a, where they are called O1 (of orientation 1), and in Fig. 15b, where they are called O2. Figure 15c shows the particle distribution that, in this case, is the same for both meshes. However, this does not mean that the support of the shape functions is precisely the same, as a result of the covering algorithm earlier presented. In this algorithm the determination of support size parameter $s$ depends on the maximum distance between the particle and its adjacent particle list, which in fact is different for each of the meshes.

For a comparison purpose, the same analysis is performed using a triangular finite element, with a tri6 element. In order to do so, the same integration meshes shown in Fig. 15a, b is used in the analysis. However, in this case the number of degrees of freedom associated with the FEM analysis is larger than those used in the MEFG analysis. The number of nodes of the FEM-tri6 mesh is 3321.

#### *6.3.1 Finite element results–Tri6*

This section presents and discusses the results obtained only by the FE analysis, using a tri6 element. Figure 16 shows the deformed meshes achieved at the end of the analysis. Figure 16a is related to the mesh with orientation O1 and Fig. 16b to the mesh with orientation O2. Figure 16c,d shows a magnification of the refined regions of the deformed configurations, shown in Fig. 16a, b respectively. The differences among the two deformed meshes are visible and arise due to the bias in the mesh and represent an example of the well known mesh-alignment problem associated with the FEM.

This difference is still more evident when the force versus displacement curve, for the top region of the body, is plotted, as shown in Fig. 17. Notice, again, that the curves are almost identical during most part of the analysis. But, at a certain point, in the necking phase, occurs an increasing difference between the values determined for the two meshes. To establish a comparison with similar works presented, for example, by Simo and Armero [26] and Souza Neto et al. [28], the results obtained by these two authors are also presented in the figure. Notice that the mesh with O2 orientation shows a better result for the force versus displacement response, when compared with the values presented by the other authors. Note also that in the PuFem tri3 case the curve behavior is almost constant after the necking threshold, that is, no necking is experience if one uses this order of PuFem approximation. Here, as explained in Sect. 2.5.2, on can see the inadequacy of the PuFem tri3 shape functions to cope with the volumetric locking phenomena.

#### *6.3.2 MEFG results*

Here, one discuss and presents the results obtained by the MEFG analysis. Figure 18 shows the deformed meshes at the end of the analysis. Figure 18a shows the integration mesh with orientation O1 and Fig 18b the mesh orientation with orientation O2. Again, Fig. 18c, d show a magnification of the more refined region of the deformed configuration, shown in Fig. 18a, b respectively. Differently to the previous example, there are no observable differences among the deformed configurations. This indicates that the solution of the problem does not have relevant integration mesh dependence.

Also, this difference is not evident in the force versus displacement curve plotted in the Fig. 19. In this graph the results obtained for the analyses with or without the incorporation of *F-bar* methodology are presented, considering the integration meshes with orientation O1 and O2, shown in Fig. 19a, b respectively. One can notice that the curves are practically identical during the entire analysis and are independent of the orientation of the cells. Again, for a comparison purpose, similar results presented by Simo and Armero [26] and Souza Neto et al. [28] are also shown in this figure.

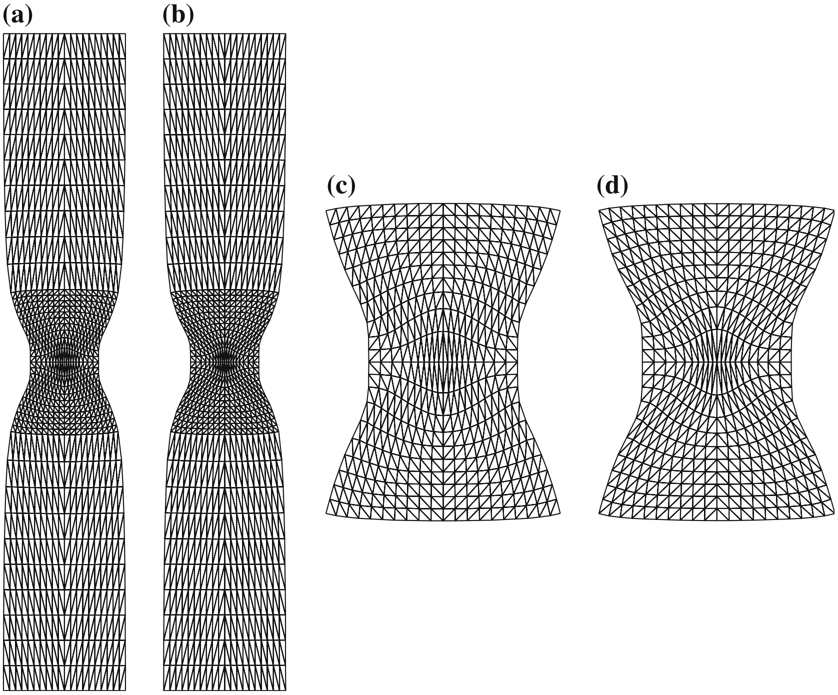

**Fig. 18** Deformed configurations, MEFG result

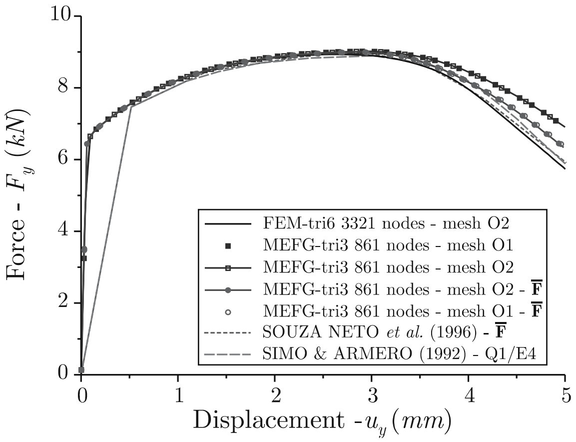

**Fig. 19** Force versus displacement at the top of the body, MEFG result

## 6.4 Stretching of a double notched specimen

This example reproduces a state of high degree of restriction due to the use of an ideal elato-plastic $J_2$ constitutive model together with the enforcement of a plane strain condition. The material parameters used in this analysis are the following ones: $\kappa = 164206.35\,\mathrm{MPa}$, $\mu = 80193.80\,\mathrm{MPa}$, $\sigma_y = 450\,\mathrm{MPa}$.

The analysis consists in the stretching of a notched body with dimensions shown in Fig. 20a. This stretching is carried out through the prescription of a displacement in the upper/lower region of the body, with no symmetry conditions imposed. In both regions a prescribed displacement of $u_y = 0.3\,\mathrm{mm}$ is applied. An incremental analysis is performed, considering 100 constant prescribed displacement steps. Figure 20b shows the integration mesh employed, considering the support parameter s = 1.5. Figure 20c shows the particle distribution. For a comparison purpose, the mesh presented in Fig. 20b is also used in FEM-tri6 and a PuFem-tri3 analysis. It is important to note that the number of degree of freedom in the FEM-tri6 is larger than the one used in the PuFem-tri3 and also MEFG analysis.

The force versus displacement curve is shown in Fig. 21. Notice that it is clear that the MEFG, without any anti-volumetric locking strategy, is not able to represent the limit load response associated with this problem. Also, the results obtained for the PuFem-tri3 and for the FEM-tri6 analysis moves away, in a drastic form, from the desired result. On the other hand, when the anti-volumetric locking strategy is used, considering two different support sizes, the limit load response is reproduced, as one can observe by the comparison with the results presented by Simo and Armero [26] and Souza Neto et al. [28]. Notice also that according with Askes et al. [4] and Huerta and Méndez [16] the size of the support, *s*, plays an important role in the volumetric locking analyses in the EFG method.

## 6.5 Cook's membrane problem

In this last example, the performance of the method is analyzed in a problem case where the bending effects are predominant. This example, known as Cook's membrane,

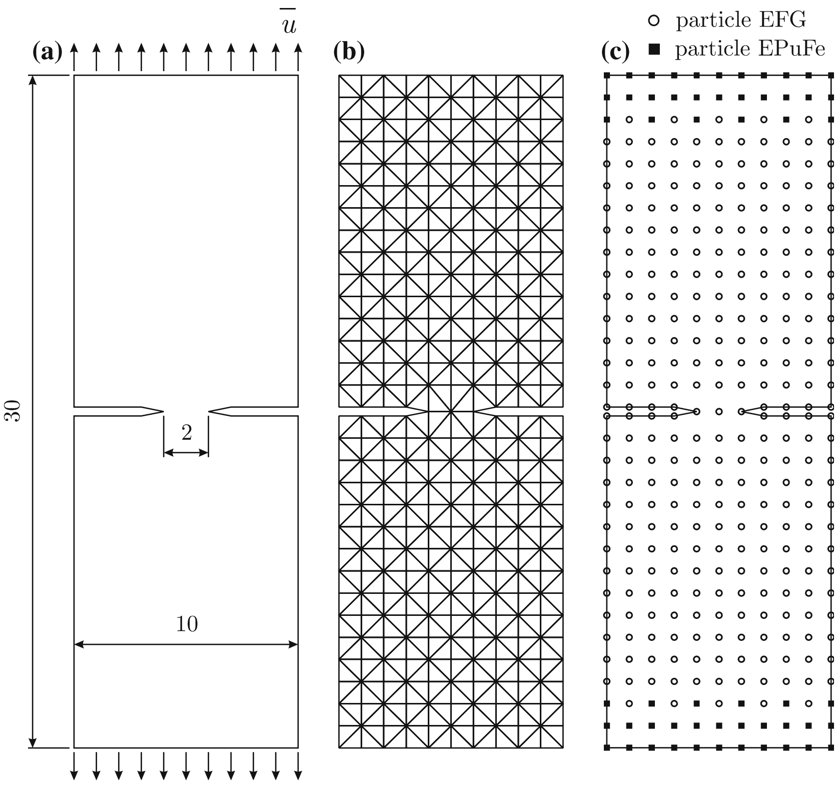

**Fig. 20** Double notched specimen model

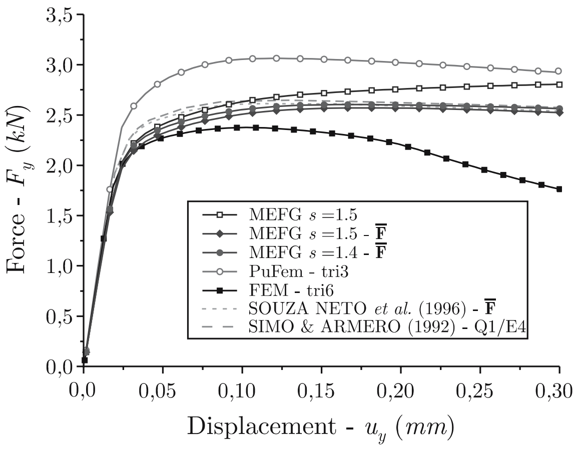

**Fig. 21** Force versus displacement at the top of the body

consists of a trapezoidal panel, under a plane strain condition, that is clamped on the left side and submitted to a shearing force of magnitude $V = 5$ kN on the right side, as illustrated in Fig. 22a. This shearing force is constant, and is distributed over the right edge, i.e., the total force applied is converted into a distributed force, given by $f = 312.5$ N/mm. The integration meshes as well as the respective particle arrangements are shown in Fig. 22.

The results for the displacement $u_y$ at the right top point of the panel versus the number of elements, distributed per side of the body, are shown in Fig. 23. Notice that, when the integration mesh is refined, the result tends to the solution of the problem, presented by Simo and Armero [26], and shown in Fig. 23.

## 7 Conclusion

In this work an element-free *Galerkin* method is numerically investigated under finite strains. Results in this paper show the necessity of using some anti-volumetric locking strategy for the MEFG method. However, the incorporation of the proposed *F-bar* approach has improved considerably the results. Moreover, Figs. 12 and Fig. 14 show that with a proper mesh refinement strategy, acting mainly in the regions subjected to high plastic flows, it is possible to reduce even more the presence of volumetric locking and improve the solution to the problem. Here, one notice that the use of the EPuFe global shape function, necessary to enforce the symmetry conditions, in the regions subjected to high plastic flows, as in the case of the necking of a circular bar, in Sect. 6.2, lead to a decrease in the accuracy of the solution to the problem, due to the loss of effectiveness of the *F-bar* methodology. The reason for this behavior is the fact that the EPuFe global shape function interpolates $\mathbf{F}$ as a constant, what makes the

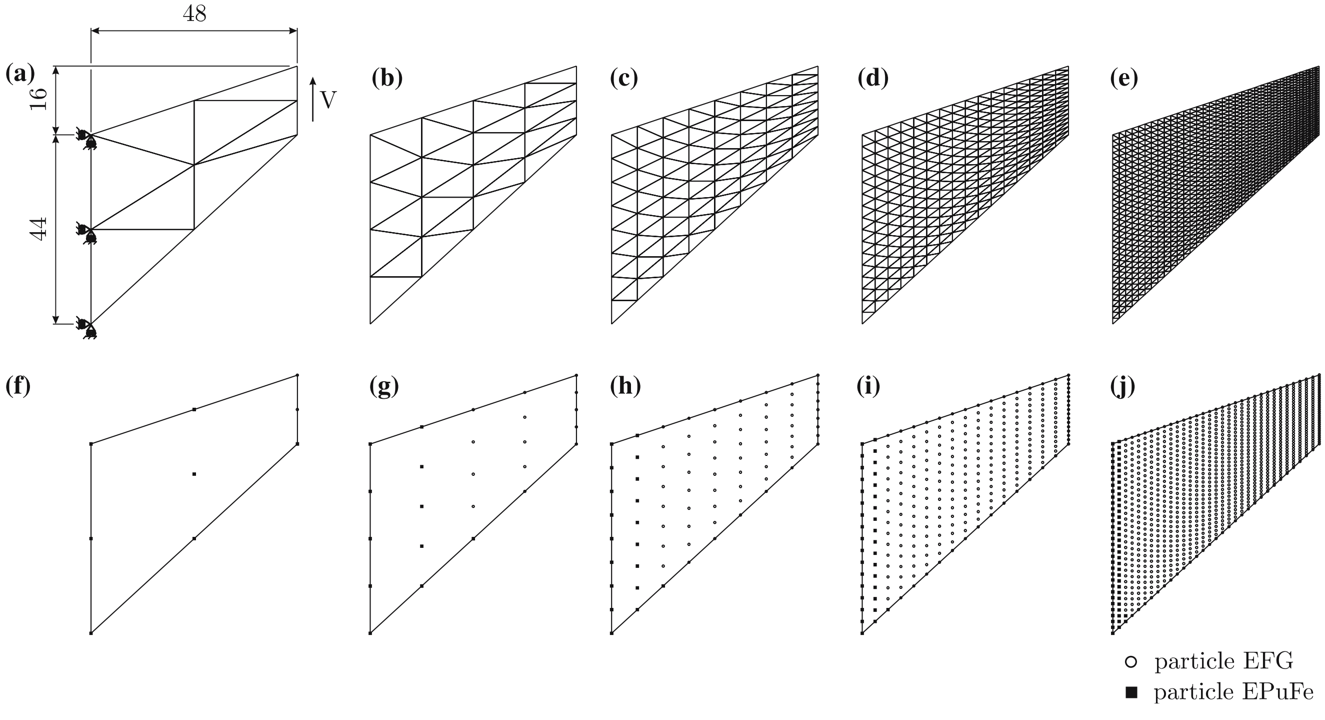

**Fig. 22** Cook's membrane model

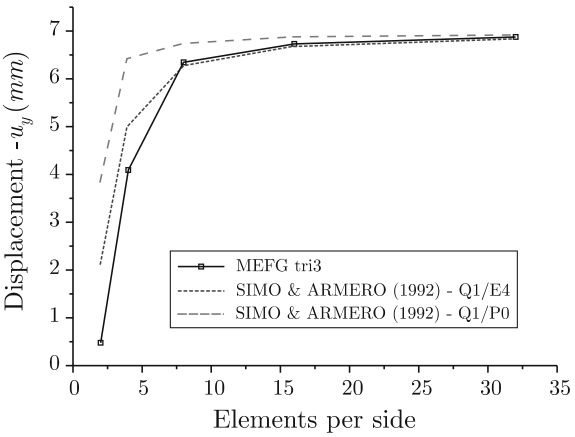

**Fig. 23** Displacement of the right superior point versus the number of elements

anti-volumetric locking strategy ineffective at the support of the EPuFe global shape function. However, this loss of accuracy can be minimized as much as required by the implementation of an *h*-adaptive mesh refinement procedure.

**Acknowledgements** The support of the CNPq, Conselho Nacional de Desenvolvimento Científico e Tecnológico, of Brazil is gratefully acknowledged. Grant Number: 304020/2003-6.

## References

1. Akkaram S, Zabaras N (2001) "An updated Lagrangian finite element sensitivity analysis of large deformations using quadrilateral elements". Int J Numer Methods Eng 52:1131–1163
2. Alves, MK, Rossi, R (2003) "A modified element-free Galerkin method with essential boundary conditions, enforced by an extended partition of unity finite element weight function". Int J Numer Methods Eng 57:1523–1552
3. Alves, MK, Rossi, R (2005) "An extension of the partition of unity finite element method. J Barz Soc Mech Sci Eng XXVII(3):209–216
4. Askes, H, De Borst, R, Heeres, O (1999) "Conditions for locking-free elasto-plastic analyses in the Element-Free Galerkin method". Comput Methods Appl Mechan Eng 173:99–109
5. Belytschko, T, Tabbara, M (1996) "Dynamic fracture using element-free Galerkin methods". Int J Numer Methods Eng 39:923–938
6. Belytschko, T, Lu, YY, Gu, L (1994) "Element-free Galerkin methods". Int J Numer Methods Eng 37:229–256
7. Belytschko, T, Organ, D, Krongauz, Y (1995) "A coupled finite element-element-free Galerkin method". Comput Mechanics 17(3):186–195
8. Dolbow, J, Belytschko, T (1999) "Volumetric locking in the element free Galerkin method". Int J Numer Methods Eng 46:925–942
9. Duarte, AC, Oden, J,T (1996) "An h-p adaptive method using clouds". Comput Methods Appl Mechanics Eng 139(1–4):237–262
10. Eterovic, AL, Bathe, KJ (1990) "A hyperelastic-based large strain elasto-plastic constitutive formulation with combined isotropic-kinematic hardening using the logarithmic stress and strain measures". Int J Numer Methods Eng 30:1099–1114
11. Gavete, L, Benito, JJ, Falcón, S, Ruiz, A (2000) "Penalty functions in constrained variational principles for element free Galerkin method". Eur J Mech A/Solids 19(4):699–720
12. Günther, FC, Liu, WK (1998) "Implementation of boundary conditions for meshless methods". Comput Methods Appl Mechanics Eng 163:205–230
13. Hegen, D (1996) "Element-free Galerkin methods in combination with finite element approaches". Comput Methods Appl Mechanics Eng 135(1–2):143–166
14. Hill R (1978) "Aspects of invariance in solid mechanics". Adv Appl Mech 18:1–75

15. Huerta, A, Méndez, SF (2000) “Enrichment and coupling of the finite element and meshless methods”. Int J Numer Methods Eng 48:1615–1636
16. Huerta, A, Méndez, SF (2001) “Locking in the incompressible limit for the element-free Galerkin method”. Int J Numer Methods Eng 51:1361–1383
17. Hughes, TJR (1980) “Generalization of seletive integration procedures to anisotropic and nonlinear media”. Int J Numer Methods Eng 15:1413–1418
18. Kaljević I, Saigal, S (1997) “An improved element free Galerkin formulation”. Int J Numer Methods Eng 40(16):2953–2974
19. Krongauz, Y, Belytschko, T (1996) “Enforcement of essential boundary conditions in meshless approximations using finite elements”. Comput Methods Appl Mechanics Eng 131(1–2):133–145
20. Lancaster, P, Salkuskas, K (1981) “Surfaces generated by moving least square methods”. Math Comput 37:141–158
21. Liu, WK, Li, S, Belytschko T (1997) “Moving least-square reproducing kernel methods (I) Methodology and convergence”. Comput Methods Appl Mechanics Eng 147:113–154
22. Ortiz M, Radovitzky, RA, Repeto, EA (2001) “The computation of exponential and logarithmic mappings and their fisrt and second linearizations”. Int J Numer Methods Eng 52:1431–1441
23. Pannachet, T, Askes, H (2000) “Some observations on the enforcement of constraint equations in the EFG method”. Commun Numer Methods Eng 16(12):819–930
24. Rossi, R, Alves, MK (2004) “Recovery Based Error Estimation and Adaptivity Applied to a Modified Element-Free Galerkin Method”. Comput Mech 33(3):194–205
25. Rossi, R, Alves, MK (2005) “An h-adaptive modified element-free Galerkin method”. Eur J Mech A/Solids 24:782–799
26. Simo, JC, Armero, F (1992) “Geometrically non-linear enhanced strain mixed methods and the method of incompatible modes”. Int J Numer Methods Eng 33:1413–1449
27. Simo, JC, Rifai S (1990) “A class of mixed assumed strain methods and the method of incompatible modes”. Int J Numer Methods Eng 29:1595–1638
28. Souza Neto EA, Peric, D, Dutko, M, Owen, DRJ (1996) “Design of simple low order finite elements for large strain analysis of nearly incompressible solids”. Int J Solids Struct 33:3277–3296
29. Souza Neto EA, Peric, D, Owen, DRJ (2002) Computational plasticity: small and large strain finite element analysis of elastic and inelastic solids. Classroom notes University College of Swansea, Wales
30. Ventura, G (2002) “An augmented Lagrangian approach to essential boundary conditions in meshless methods”. Int J Numer Methods Eng 53:825–842
31. Vidal, Y, Villon, P Huerta, A (2003) “Locking in the incompressible limit:pseudo-divergence-free element free Galerkin”. Commun Numer Methods Eng 19:725–735
32. Weber G, Anand, L (1990) “Finite deformation constitutive equations and a time integration procedure for isotropic” hyperelastic-viscoplastic solids. Comput Methods Appl Mechanics Eng 79:173–202
33. Wells, GN, Sluys, LJ, De Borst, R (2002) “A *p*-adaptive scheme for overcoming volumetric locking during plastic flow”. Comput Methods Appl Mechanics Eng 191:3153–3164
34. Zhang, X, Liu, X, Song, KZ, Lu, MW (2001) “Imposition of essential boundary conditions by displacement constraint equations in meshless methods”. Commun Numer Methods Eng 17(3): 165–178
35. Zhu, T, Atluri, N (1998) “Modified collocation method and a penalty function for enforcing the essential boundary conditions in the element free Galerkin method”. Comput Mech 21: 211–222